

1 Predicting the roughness length of turbulent flows over
2 landscapes with multi-scale microtopography

3 **Jon D. Pelletier*** and **Jason P. Field**

4 *Department of Geosciences, University of Arizona, Gould-Simpson Building, 1040 East Fourth*
5 *Street, Tucson, Arizona 85721-0077, USA*

6 **corresponding author; email: jdpellet@email.arizona.edu*

7
8 **Abstract**

9 The fully rough form of the law of the wall is commonly used to quantify velocity
10 profiles and associated bed shear stresses in fluvial, aeolian, and coastal environments. A key
11 parameter in this law is the roughness length, z_0 . Here we propose a predictive formula for z_0 that
12 uses the amplitude and slope of each wavelength of microtopography within a discrete-Fourier-
13 transform-based approach. Computational fluid dynamics (CFD) modeling is used to quantify
14 the effective z_0 value of sinusoidal microtopography as a function of the amplitude and slope.
15 The effective z_0 value of landscapes with multi-scale roughness is then given by the sum of
16 contributions from each Fourier mode of the microtopography. Predictions of the equation are
17 tested against z_0 values measured in $\sim 10^5$ wind velocity profiles from southwestern U.S. playa
18 surfaces. Our equation is capable of predicting z_0 values to 50% accuracy, on average, across a
19 four order-of-magnitude range. We also use our results to provide a simpler alternative formula
20 that, while somewhat less accurate than the one obtained from a full multi-scale analysis, has an
21 advantage of being simpler and easier to apply.

22 *Keywords: boundary layer flow, law of the wall, roughness length, terrestrial laser scanning,*
23 *computational fluid dynamics (CFD)*

24

25 **1. Introduction**

26 **1.1. Problem statement**

27 The velocity profiles of turbulent boundary-layer flows are often quantified using the
28 fully rough form of the law of the wall:

$$29 \quad u(z) = \frac{u_*}{\kappa} \ln\left(\frac{z}{z_0}\right). \quad (1)$$

30 where $u(z)$ is the wind velocity (averaged over some time interval) at a height z above the bed, u_*
31 is the shear velocity, κ is the von Kármán constant (0.41), and z_0 is an effective roughness length
32 that includes the effects of grain-scale roughness and microtopography (e.g. Bauer et al., 1992;
33 Dong et al., 2001). Velocity profiles measured in the field are commonly fit to equation (1) to
34 estimate u_* and/or τ_b for input into empirical sediment transport models (often after a
35 decomposition of the bed shear stress into skin and form drag components) (e.g. Gomez and
36 Church, 1989; Nakato, 1990). Fits of wind-velocity profiles to equation (1) also provide
37 measurements of z_0 . Given a value for z_0 , a time series of u_* and/or τ_b can be calculated from
38 equation (1) using measurements of velocity from just a single height above the ground. This
39 approach is widely used because flow velocity data are often limited to a single height. Equation
40 (1) only applies to $z \geq z_0$, and may be further limited in its accuracy within the roughness
41 sublayer, i.e. the range of heights above the ground comparable to the height of the largest
42 roughness elements. The roughness sublayer is the layer where the mean velocity profile deviates
43 from the law of the wall as the flow interacts with individual roughness elements. This layer is
44 typically considered to extend from the ground surface to a height of approximately twice the

45 height of the tallest roughness elements. Values of z_0 depend on microtopography/land cover
46 (quantifying this dependence in unvegetated landscapes is a key goal of this paper) and are
47 typically in the range of 10^{-2} - 10^1 mm for wind flow over arid regions (Prigent et al., 2005).

48 Most existing methods for estimating z_0 using metrics of surface roughness or
49 microtopography rely on the concept of a dominant roughness element, the size and density of
50 which the user must specify *a priori* (e.g. Lettau, 1969; Arya, 1975; Smith and McLean, 1977;
51 Jacobs, 1989; Taylor et al., 1989; Raupach, 1992; 1994; Kean and Smith, 2006a). Procedures are
52 available for estimating z_0 in landscapes with multi-scale roughness, but they often rely on
53 idealizations such as treating the microtopography as a sequence of Gaussian bumps (e.g. Kean
54 and Smith, 2006b). Nearly all natural landscapes have microtopographic variability over a wide
55 range of spatial scales. Identifying the dominant scale objectively and uniquely can be difficult.
56 For example, the top plot in Figure 1 shows a hypothetical case of a landscape composed of two
57 superposed sine waves. The effective roughness length of a landscape is related to the
58 presence/absence or extent of flow separation, and flow separation is primarily controlled by the
59 derivatives of topography (slope and curvature) rather than the amplitude of the
60 bedforms/roughness elements (Simpson, 1989; Lamballais et al., 2010). As such, roughness
61 elements of smaller amplitude but steeper slopes may exert greater control on z_0 values compared
62 with roughness elements that are larger in amplitude but gentler in slope. Given a landscape with
63 multi-scale roughness in which each scale has distinct amplitudes and slopes, it can be difficult
64 to identify the dominant scale or scales of roughness for the purposes of estimating z_0 .

65 Figure 1 illustrates two examples of microtopography from playa surfaces in the
66 southwestern U.S. The middle plot shows a transect through the Devil's Golf Course in Death
67 Valley, California and the bottom plot shows a transect through a relatively smooth section of

68 Lordsburg Playa, New Mexico. These plots are presented using different vertical scales because
69 the amplitude of the microtopography at the Death Valley site is approximately 100 times greater
70 than that of the Lordsburg Playa site. Both landscapes have no vegetation cover, no loose sand
71 available for transport, and are flat or locally planar at scales larger than ~1 m. As such, they are
72 among the simplest possible natural landscapes in terms of their roughness characteristics.
73 Nevertheless, as Figure 1 demonstrates, they are characterized by significant roughness over all
74 spatial scales from the resolution of the data (1 cm) up to spatial scales of ~1 m. To our
75 knowledge, there is no procedure for predicting z_0 in a way that honors the multi-scale nature of
76 microtopography in real cases such as these. To meet this need, we have developed and tested a
77 discrete-Fourier-transform-based approach to quantifying the effects of microtopographic
78 variations on z_0 values. The method simultaneously provides an objective measure of the spatial
79 scales of microtopography/roughness that most strongly control z_0 .

80 In a recent paper similar in spirit to this one, Nield et al. (2014) quantified the z_0 values of
81 wind velocity profiles over playas as a function of various microtopographic metrics. Nield et al.
82 (2014) proposed an empirical, power-law relationship between z_0 and the root-mean-squared
83 variations of microtopography, H_{RMSE} :

$$84 \quad z_0 = cH_{RMSE}^{1.66} \quad (2)$$

85 where the coefficient c is equal to $\ln(-1.43)$ or $0.239 \text{ m}^{-0.34}$. Equation (2) is one example of
86 several predictive formulae that Nield et al. (2014) proposed for different surface types (equation
87 (2) applies to surfaces with large roughness elements or that exhibit mixed homogenous patches
88 of large and small roughness elements). Nield et al. (2014) concluded that “the spacing of
89 morphological elements is far less powerful in explaining variations in z_0 than metrics based on
90 surface roughness height.” In this paper we build upon the results of Nield et al. (2014) to show

91 that z_0 can be most accurately predicted using a combination of the amplitudes and slopes of
92 microtopographic variations.

93 The presence of multi-scale roughness in nearly all landscapes complicates attempts to
94 quantify effective z_0 values for input into regional and global atmospheric and Earth-system
95 models. In such models, topographic variations are resolved at scales larger than a single grid
96 cell (10-100 km at present, but steadily decreasing through time as computational power
97 increases) but the aerodynamic effects of topographic variations on wind velocity profiles at
98 smaller scales are not resolved in these models and must be represented by an effective z_0 value
99 (sometimes in combination with an additional parameter, the displacement height, which shifts
100 the location of maximum shear stress to a location close to the top of the roughness sublayer
101 (Jackson, 1981)). Topographic variations at spatial scales below 10-100 km are typically on the
102 order of tens to hundreds of meters. Currently available maps of z_0 values do not incorporate the
103 aerodynamic effects of topography at such scales. For example, Prigent et al. (2005) developed a
104 global map of z_0 in deserts by correlating radar-derived measurements of decimeter-scale
105 roughness with z_0 values inferred from wind velocity profiles. This approach assumes that the
106 dominant roughness elements that control the effective z_0 value over scales of 10-100 km occur
107 at the decimeter scale captured by radar. It is possible that, in some landscapes, the roughness
108 that controls z_0 occurs at scales that are larger or smaller than those measured by radar.
109 Therefore, a procedure is needed that predicts z_0 values using data for topographic variations
110 over a wide range of scales, including but not limited to decimeter scales. This study aims to fill
111 that gap.

112 **1.2. Study Sites**

113 We collected wind-velocity profiles and high-resolution topographic data using terrestrial
114 laser scanning (TLS) from ten playa sites in the southwestern U.S. (Fig. 2) during the spring of
115 2015. These sites were selected based on the range of microtopographic roughness they exhibit
116 (Table 1). Roughness can be quantified in multiple ways, but H_{RMSE} , the root-mean-squared
117 deviation of elevation values measured at a sampling interval of 0.01 m, provides one
118 appropriate metric (Nield et al., 2014). The ten sites range in H_{RMSE} from approximately 0.55
119 mm to 36 mm (see Section 2.1). In addition to the H_{RMSE} we computed S_{av} , the average slope
120 computed at 0.01 m scale, for each site. Values of S_{av} range from 0.01 to 0.159 (Table 1).

121 Each study site was an area of at least 30 m x 30 m with relatively uniform roughness, as
122 judged visually and by analysis of the TLS data. The minimum fetch required for an equilibrium
123 boundary layer flow is typically assumed to be 1000 times the height of the dominant roughness
124 elements (Counihan, 1971). Based on this criterion, 30 m was adequate fetch for seven of the ten
125 sites, i.e. all except for the three Death Valley sites, where roughness elements were up to 300
126 mm, hence the area of homogeneous roughness was verified to a distance of only ~ 100 times the
127 height of the dominant roughness elements. However, the required fetch must also depend on the
128 maximum height above the ground where velocities are measured to compute a z_0 value locally,
129 since any roughness transition triggers an internal boundary layer that grows indefinitely in
130 height with increasing distance downwind of the transition. Using the Elliot (1958) formula for
131 the height of the internal boundary layer downwind of a roughness transition, the minimum fetch
132 required for an log-law profile between 0 and 3 m above the ground over a landscape with $z_0 \approx$
133 30 mm (the value measured at the Death Valley rough site) is 31.8 m. According to this
134 alternative criterion, 30 m may be adequate for an equilibrium boundary layer flow to be

135 established to a height of 3 m despite the limited fetch-to-roughness height ratio at the Death
136 Valley sites.

137 The playa surfaces at our study sites were predominantly crusted and ranged from flat,
138 recently formed crust to well-formed polygons with deflated and broken crust ridges. All of the
139 sites were completely devoid of vegetation. Sand blows episodically across some portions of the
140 playas we studied but we chose study areas in which we observed no sediment transport during
141 fast winds. We considered only landscapes without vegetation and loose, erodible sand because
142 such cases must be understood first before the additional complications of flexible roughness
143 elements and saltation-induced roughness can be tackled. That said, we anticipate that concepts
144 from this paper may be relevant to quantifying z_0 over vegetated landscapes also.

145 Our goal is to understand the controls on boundary layer flows over rough terrain
146 generally, not playa surfaces specifically or exclusively. As such, we use playa surfaces as
147 “model” landscapes. Playas are useful for this purpose because they are macroscopically flat but
148 exhibit a wide range of microtopographic roughness at small scales. The relative flatness of
149 playas at scales larger than ~1 m makes it possible to characterize their boundary layer flows
150 using relatively short anemometer towers. Of course, playas are also of special interest to aeolian
151 geomorphologists because they can be major dust sources when sand from playa margins is
152 transported across the playa surface, disturbing crusted surfaces and liberating large volumes of
153 silt- and clay-rich sediments.

154 The questions addressed in this paper could, in principle, be addressed using wind tunnel
155 experiments. Wind tunnels certainly have the advantage of user control over wind velocities.
156 However, Sherman and Farrell (2008) documented that z_0 values in wind tunnels are, on average,
157 approximately an order of magnitude lower than those measured in the field for otherwise similar

158 conditions (e.g. grain size). One interpretation of the Sherman and Farrell (2008) results is that
159 the confined nature of wind tunnel flows and/or their limited fetch can limit the development of
160 boundary layers in equilibrium with bed roughness. For this reason, we focused on measuring
161 wind flow over natural surfaces with homogeneous roughness characteristics over distances of at
162 least 30 m surrounding our measurement locations.

163

164 **2. Methods**

165 **2.1. Terrestrial laser scanning and analyses of playa surface microtopography**

166 A Leica C10 terrestrial laser scanner was used to acquire point clouds of the central 10 m
167 x 10 m ground surface upwind of the anemometers at each of the 10 study sites. The areas
168 surrounding each 10 m x 10 m area were also surveyed to check for approximate homogeneity in
169 the roughness metrics out to areas of 30 m x 30 m, but the central 10 m x 10 m areas were the
170 focus of the subsequent data analysis. Each area was scanned from four stations surrounding the
171 10 m x 10 m area and merged into a single point cloud using a Leica disk target system.
172 Registration errors were a maximum of 2 mm in all cases. The Leica C10 has an inherent
173 surface-model accuracy of 2 mm, but this value decreases as the number of overlapping scans
174 increases (Hodge, 2010), resulting in a value of approximately 1 mm in the case of four
175 overlapping scans. The scanner was mounted on a 3.5 m tripod to maximize the angle of
176 incidence (low angles of incidence elongate the “shadows” or occlusions behind
177 microtopographic highs (Brown and Hugenholtz, 2013)). All of the returns within each 1 cm²
178 domain were averaged to create a Digital Elevation Model (DEM) with point spacing of 0.01 m.
179 Voids were filled using natural-neighbor interpolation. Voids requiring interpolation were
180 limited to <1% of the area at the smoothest five sites (Lordsburg and Willcox Playas), between

181 1% and 3% at the two Soda Lake sites, and between 10% and 20% at the three Death Valley
182 sites.

183 In addition to the calculation of basic topographic metrics such as H_{RMSE} and S_{av} (the
184 latter being the average slope computed at 0.01 m scales) (Table 1), we also computed the
185 average amplitude spectrum of all 1D topographic transects at each study site. The amplitude
186 spectrum is equal to two times the absolute value of the complex discrete Fourier transform
187 (DFT). The average amplitude spectrum refers to the fact that the one thousand amplitude
188 spectra of each 1D transect computed along the east-west direction were averaged to obtain a
189 single average spectrum for each study site. We used the DFT implemented in the IDL
190 programming language. The DFT coefficients were also used as input to a filter that uses the
191 amplitude and slope of each Fourier mode to compute its contribution to the z_0 value. We created
192 “mirror” images of each transect before application of the DFT. This approach has been shown
193 to work as well or better than windowing for minimizing truncation error (i.e. incomplete
194 sampling) in data sets characterized by the broadband/multi-scale variability characteristic of
195 many environmental data series (Smigelski, 2013).

196 **2.2. Measurement and analyses of wind profiles**

197 Wind speeds were measured at 1 s intervals and at 7 heights above the surface (0.01 m,
198 0.035 m, 0.076 m, 0.16 m, 0.52 m, 1.22 m, and 2.80 m) using four Inspeed Vortex rotating cup
199 anemometers and four AccuSense hotwire anemometers (F900 series) (the latter calibrated to
200 work over the 0.15-10 m s⁻¹ range of wind velocities) (Fig. 3). The hotwire sensors were secured
201 to an L-shaped steel frame and placed above the surface such that the small opening in the sensor
202 head was oriented as perpendicular to the wind direction as possible (Fig. 3). The 10 m s⁻¹ range
203 of the hotwire sensors was not a limiting factor because all of the hot-wire sensors were located

204 close to the ground, i.e. within 0.16 m from the surface, where velocities were lower than 10 m s^{-1}
205 ¹ during our deployments. We collected data at each of the ten sites for ten to thirty hours
206 spanning multiple days, times of day, and a wide range of wind velocities.

207 The lowest cup and the highest hotwire anemometers were positioned at the same height
208 (0.16 m) above the surface to standardize measurements between the two types of wind sensors.
209 When positioned at the same height, the hotwire sensors measured wind speeds (based on the
210 factory calibration) that were approximately 10% lower than the values obtained from the cup
211 anemometers. We used the ratio of the wind velocities measured by the bottom cup anemometer
212 to the wind velocities measured by the top hotwire sensor to standardize the hotwire
213 measurements to the cup anemometer measurements in real time. This scaling-factor approach
214 also serves a second purpose, which is to minimize the effects of wind-direction variability on
215 the velocities measured by the hotwire sensors. The cup sensors measure wind speeds effectively
216 from nearly any direction, but the hotwire sensors are required to be oriented within 20°
217 perpendicular to the wind for greatest accuracy. The hotwires were manually repositioned
218 following large and sustained changes in wind direction, but short-duration changes may have
219 resulted in oblique incidence angles with a bias towards lower velocities. Continually rescaling
220 the velocities measured by the highest hotwire sensor to the lowest cup sensor mitigated this
221 potential problem.

222 Scaled values from the bottom three (0.01 m, 0.035 m, and 0.076 m) hotwire sensors
223 were combined with the four cup anemometers to calculate shear velocities, u_* , and aerodynamic
224 roughness lengths, z_0 , based on the average velocities measured in each 12-s interval via least-
225 squares fitting of the wind velocities to the natural logarithm of the distance above the ground.
226 To extract a z_0 value from the velocity profile data, we followed the procedure of Bergeron and

227 Abrahams (1992), who emphasized the need to regress u on $\ln z$ rather than $\ln z$ on u . The shear
228 velocity is equal to the slope of the regression of u on $\ln z$ multiplied by κ (equation (6) of
229 Bergeron and Abrahams (1992)) and the roughness length is equal to the exponential of the
230 following: minus the intercept divided by the slope (equation (7) of Bergeron and Abrahams
231 (1992)). The 12-s interval was chosen based on the results of Nimakas et al. (2003), who found
232 that time intervals greater than 10 s resulted in the most accurate results, while those obtained
233 from smaller averaging intervals were less reliable. Values of z_0 can be influenced by deviations
234 from neutral stability. A common way to address this issue is to remove profiles from the
235 analysis in which the velocity at a given height is below some threshold value (e.g. Nield et al.,
236 2014). In this study we repeated our analysis using only those profiles with a wind velocity of at
237 least 3 m s^{-1} at a height of 0.16 m. The mean and standard deviations of z_0 were nearly identical
238 to those obtained using all of the data, likely reflecting the fact that we targeted time periods of
239 fast winds for measurement.

240 During the data collection, the hotwire sensors were moved to approximately 25-50
241 random locations within each site. We moved the hotwire sensors to numerous locations within
242 each site because wind velocities measured close to the ground are sensitive to the
243 microtopography of the specific spot above which they are measured, i.e. the z_0 value measured
244 on the stoss side of a microtopographic high tends to be smaller than the z_0 value measured on
245 the lee due to the convergence/divergence of flow lines. Since our goal was to characterize the
246 average or representative z_0 value over each surface, it is appropriate to move the hotwire sensors
247 around the surface to ensure that the results are not specific to one location but instead represent
248 a statistical “sample” of the flow above the surface at multiple locations. This approach is also
249 consistent with how the CFD model output was analyzed (see Section 2.3).

250 Velocity profiles can deviate from equation (1) close to the ground over rough terrain. As
251 such, it is important to identify which sensors, if any, are located within the roughness sublayer
252 prior to computing u_* and z_0 values by fitting wind velocity data to equation (1). To do this, we
253 plotted the average of all wind velocity measurements at each site as a function of $\ln z$. The
254 results (described in Section 3.2) show that the lowest two (hotwire) sensors (located 0.10 and
255 0.035 m above the ground) at the three Death Valley sites and the rough Soda Lake site deviated
256 noticeably from equation (1). The fact that these sensors were within the roughness sublayer is
257 consistent with the fact that the height of the largest roughness elements at these sites is greater
258 than or comparable to 0.035 m (the height of the second lowest sensor). Data from the lowest
259 sensor at the next four smoothest sites (i.e. smooth Soda Lake, the two Willcox Playa sites, and
260 the rough Lordsburg Playa site) also deviate noticeably from equation (1). Data from these
261 sensors were not used in the calculation of u_* and z_0 at those sites. In addition, we verified in all
262 cases that the removal of these sensors deemed to be within the roughness sublayer improved the
263 mean correlation coefficients, R^2 , at each site. Only profiles with R^2 values greater than 0.95
264 were retained.

265 **2.3. Computational fluid dynamics**

266 CFD modeling was used to quantify the effects of the amplitude and slope of sinusoidal
267 microtopography on z_0 . We used the 2013 version of the PHOENICS CFD model (Ludwig,
268 2011) to estimate the time-averaged wind velocities associated with neutrally stratified turbulent
269 flow over sinusoidal topography with a range of amplitudes and slopes. PHOENICS uses a
270 finite-volume scheme to solve simultaneously for the time-averaged pressure and flow velocity.
271 PHOENICS solves the flow equations using the iterative SIMPLEST algorithm of Spalding
272 (1980), which is a variant of the SIMPLE algorithm of Patankar and Spalding (1972). The

273 solution was considered converged when the state variables changed by less than 0.001% from
274 one iteration to the next. We used the renormalization group variant of the k - ϵ closure scheme
275 first proposed by Yakhot and Orszag (1986) and later updated by Yakhot et al. (1992), which is
276 widely used for sheared/separated boundary layer flows.

277 Inputs to our model runs include a topographic profile (in these cases, a sinusoid of a
278 prescribed amplitude and maximum slope), a grain-scale roughness length, z_{0g} (set to be 0.003
279 mm for all runs), and a prescribed horizontal velocity at a reference height far from the bed ($u_r =$
280 10 m s^{-1} at $z_r = 10 \text{ m}$ was used for all of the model runs presented). The value of z_{0g} was chosen
281 based on the measured value of z_0 at the two flattest sites (Lordsburg smooth and intermediate),
282 both of which yield $z_0 = 0.002 \text{ mm}$ as described in Section 3.2. This value is also consistent with
283 the grain-scale roughness expected at a site with a median grain size of fine sand if the Bagnold
284 (1938) relation $z_{0g} = d_{50}/30$ is used. The ground surface is prescribed to be a fully rough
285 boundary, i.e. one that results in a law of the wall velocity profile characterized by a roughness
286 length equal to z_{0g} (0.003 mm) and a shear velocity equal to $\kappa u_r / \ln(z_r/z_{0g})$ (0.26 m s^{-1}) in the
287 absence of topography. In the CFD model the ground surface is treated using a wall-function
288 approach, i.e. the velocity profile within the first cell is assumed to be logarithmic with a
289 microscale roughness length equal to z_{0g} if the flow is turbulent, otherwise a laminar profile is
290 used based on the viscosity of air. At the upwind boundary of the model domain an “inlet” law of
291 the wall velocity profile is prescribed with a roughness length equal to z_{0g} . At the downwind
292 boundary (i.e. the “outlet”) a fixed-pressure boundary condition is used.

293 The computational grids we used consisted of 2D terrain-following coordinate systems.
294 Thirty logarithmically spaced grid points were used in the vertical direction, ranging from 0.1
295 mm to 10 m above the bed. We used 2000 grid points in the horizontal direction. The absolute

296 size of the horizontal domain varied depending on the slope of the bedforms. That is, the
297 topographic profile was identical for all of the runs (except for the fact that an amplitude of 0.05
298 m used for half of the runs and an amplitude of 0.1 m was used for the other half). Steeper slopes
299 were obtained by decreasing the horizontal grid spacing or “compressing” the input topographic
300 profile horizontally. The minimum length/fetch of the model domain was 30 m. Our analysis of
301 the wind profiles output by the model was restricted to the last 20% of the model domain, i.e. the
302 portion farthest downwind. This was necessary because the upwind boundary of the model is a
303 roughness transition triggered by the interaction of the input velocity profile (characterized by
304 roughness length z_{0g}) with the microtopography. This roughness transition generates an internal
305 boundary layer that grows with distance from the upwind end of the domain. Within the internal
306 boundary layer, the velocity profile is characterized by an effective roughness length z_0 set by the
307 amplitude and slope of the bedforms. To properly compute the value of z_0 based on velocity
308 profiles from the top of the roughness sublayer to a height of 3 m, it is necessary to restrict the
309 analysis of the wind profiles to the downwind end of a model domain that is at least 30 m in
310 length as described in Section 1.2.

311 Model runs were performed using two different amplitudes (0.05 and 0.1 m) and a range
312 of maximum slopes from 0.001 to 2.0. Each of the four hundred vertical velocity profiles of the
313 last 20% of the model domain were fit to equation (1) from the top of the roughness sublayer
314 (assumed to be equal to twice the maximum height of the bedforms) to a height of 3 m (to match
315 the maximum height measured in the field). The four hundred z_0 values were then averaged to
316 obtain an effective z_0 value for each value of the sinusoidal amplitude and slope. Values of z_0
317 were fit to the expression

$$318 \quad z_0 = z_{0g} + \frac{c_1 a}{1 + (c_2/S)^{c_3}}, \quad (3)$$

319 where a is the amplitude (in units of m) of the sinusoid, S is the maximum slope (the slope at the
320 point of inflection of the sinusoid in units of m/m), and c_1 , c_2 , and c_3 are unitless coefficients.

321 **2.4. Fourier analysis of topography and a multi-scale approach to quantifying z_0**

322 The results of the CFD modeling (described in Section 3.3) suggest that the slope and
323 amplitude of microtopographic variations control z_0 values via the sigmoidal relation of equation
324 (3). This result provides a basis for quantifying the multi-scale controls on z_0 within a discrete-
325 Fourier-transform-based approach that treats each Fourier mode as a sinusoid, uses equation (3)
326 to quantify the effective roughness associated with each sinusoid, and then sums the
327 contributions of each sinusoid to determine the total effective z_0 value, fully taking into account
328 microtopographic variations across a wide range of scales.

329 Within the implementation of the DFT in the IDL programming language, the amplitude
330 of each Fourier mode is equal to 2 times the amplitude of the complex Fourier coefficient, i.e. a_n
331 $= 2|f_n|$, and the maximum slope is given by $S_n = 2\pi k a$, where k is the natural wavenumber. As
332 such, the generalization of equation (4) to multiscale topography as quantified using the DFT is

$$333 \quad z_0 = z_{0g} + \sum_{n=1}^N z_{0n} \quad \text{where} \quad z_{0n} = \frac{2c_4 |f_n|}{1 + (c_2 / |4\pi k f_n|)^{c_3}}. \quad (4)$$

334 where c_4 is a unitless coefficient analogous to c_1 but with a potentially different value, and k is
335 the natural wavenumber defined as the inverse of the wavelength. We verified that equation (4)
336 returns the same value of z_0 as predicted by equation (3) for the case of a sinusoidal bed if $c_4 =$
337 c_1 . We also verified that the z_0 values predicted by equation (4) were independent of the total
338 number of data points and the sampling interval of the input data (provided that the dominant
339 scales of roughness were represented and resolved). The best-fit value of c_4 was obtained by a
340 brute-forced trial-and-error minimization of the least-squared difference between the predictions
341 of equation (4) and the mean z_0 values measured at the ten sites.

342 An alternative approach to equation (4) that is easier to apply and does not rely on the
343 Fourier transform is

$$344 \quad z_0 = z_{0g} + c_5 H_{\text{RMSE}} S_{\text{av}}^{c_6}, \quad (5)$$

345 where c_5 and c_6 are unitless coefficients.

346

347 **3. Results**

348 **3.1. TLS surveying**

349 Figure 4 presents color maps of the topography of the roughest and smoothest sites at
350 each playa. Table 1 presents summary statistics for the ten sites, including the topographic
351 metrics H_{RMSE} and S_{av} .

352 Figure 5 plots the average amplitude spectrum of all 1D topographic transects for each
353 site. These spectra demonstrate that significant topographic variability exists at all spatial scales
354 of measurement, i.e. from 0.02-10 m (note that two samples are required for Fourier analysis,
355 hence the smallest wavelength captured in our analysis is $2\Delta x$ or 0.02 m). A surface with a single
356 scale of roughness, such as wind ripples, would have power concentrated at a narrow range of
357 wavelengths, unlike the “broadband” spectra of Figure 5. Also, note that the different shapes of
358 the spectra reflect the different spatial scales that dominate topographic variability at each site.
359 At Willcox Playa, for example, the largest roughness elements occur at horizontal spatial scales
360 ~1-3 m (Figs. 4D&4E). As a result, the power spectra for the Willcox sites exhibit a “bend” at
361 wavelengths of approximately 1-3 m, indicating that the amplitude of the microtopography drops
362 off substantially at wavenumbers larger than 0.3-1, i.e. wavelengths smaller than 1-3 m. A
363 similar bend occurs in the Lordsburg rough site but at a higher wavenumber corresponding to a

364 wavelength of $\sim 0.03\text{-}0.1$ m. The color map of the Lordsburg rough site is consistent with this, i.e.
365 it shows a “dimpled” surface with large roughness elements $\sim 0.03\text{-}0.1$ m in size.

366 **3.2. Measurement and analyses of wind profiles**

367 Figure 6 plots the relationship between the average wind velocity (normalized to the
368 value measured at 2.8 m above the ground) and the natural logarithm of height above the ground
369 for all sites. The data have been normalized to emphasize how z_0 and deviations from equation
370 (1) vary among the sites (neither of which depend on absolute velocity values). Note that the
371 three Death Valley sites have been shifted to the left along the x axis by 0.1 m s^{-1} to help
372 differentiate the plots.

373 The law of the wall predicts a constant slope when u is plotted vs. $\ln z$. When the
374 velocities are normalized as in Figure 6, a steeper slope corresponds to a smaller z_0 value. The
375 slopes of the lines in Figure 6 systematically decrease (hence mean z_0 values increase) from the
376 smoothest playa (Lordsburg) to the roughest (Death Valley). Within each playa, the slopes also
377 systematically decrease from relatively smooth sites to rough sites (Table 1). The plots in Figure
378 6 suggest that the lowest two sensors (located 0.01 and 0.035 m above the ground) at the Death
379 Valley sites and the rough Soda Lake site reside within the roughness sublayer and hence should
380 not be used to obtain z_0 values via least-squares fitting of data to equation (1). The same is true
381 for the lowest sensor at the four smoother sites (all but the two smoothest sites at Lordsburg
382 Playa).

383 Histograms of z_0 values measured at each site are presented in Figures 7A&7C. As noted
384 in section 2.2, a z_0 value was calculated for each 12 s interval for which a least squares fit of u to
385 $\ln z$ yielded a R^2 value of greater than 0.95. Figure 7 shows that z_0 values are approximately
386 lognormally distributed. Sites that have higher-amplitude microtopographic variations at the 0.01

387 m scale (as measured by the average amplitude spectra in Figure 5) have higher z_0 values. Aside
388 from measurement error/uncertainty, there are two reasons for variance in measured z_0 values.
389 The first is the fluctuating nature of turbulence itself. This source of variance can be reduced by
390 averaging the wind velocities over longer time intervals before fitting to equation (1). The
391 second source of variance comes from moving the hotwire sensors to different locations around
392 each site, thereby “sampling” different patches of microtopography. We found this second source
393 to be the dominant source of variation based on the fact that z_0 values exhibit much greater
394 variability over time scales of ~ 1 h, i.e. the time scale over which the hot-wire sensors were
395 moved around the landscape.

396 Values of mean z_0 for each site have a power-law dependence on H_{RMSE} (Fig. 8A), i.e.

$$397 \quad z_0 = cH_{\text{RMSE}}^b \quad (6)$$

398 where $c = 6 \pm 1 \text{ m}^{-1}$ and $b = 2.0 \pm 0.1$ and the uncertainty values represent 1σ standard
399 deviations. Equation (6) is broadly consistent with the results of Nield et al. (2014) (equation
400 (2)). The value of the exponent b we obtained is slightly higher than that of Nield et al. (2014),
401 but such a difference is not unexpected considering that we are studying different playas.

402 There are several limitations with using H_{RMSE} as the sole or primary predictive variable
403 for z_0 . First, a nonlinear relationship between z_0 and H_{RMSE} yields unrealistic values when applied
404 outside the range of spatial scales considered here and in Nield et al. (2014). For example, using
405 equation (6) with H_{RMSE} values in the range of predicts z_0 values in the range of 6-54 m, i.e.
406 values larger than any value ever measured. Playa surfaces rarely, if ever, have H_{RMSE} values of
407 1-3 m, but many other landscapes (e.g. alluvial fans) do. Since the goal of this work is to use
408 playas as model landscapes for understanding the multi-scale controls on z_0 above landscapes in
409 general (not playas specifically), it is necessary for any empirical equation to predict reasonable

410 results for a broad range of landscape types and a range of spatial scales beyond the specific
411 range considered in the model calibration. Second, H_{RMSE} values are problematic to use as the
412 sole or dominant variable for use in predicting z_0 values because they contain no information
413 about terrain slope. A topographic transect with a point spacing of 0.01 m can be “stretched” to
414 obtain any slope value, with importance consequences for flow separation and z_0 values.

415 Figure 8B plots the relationship between mean z_0 and S_{av} , the mean slope computed
416 between adjacent points at the 0.01 m scale, for the ten study sites. This figure documents a
417 systematic nonlinear relationship between z_0 and S_{av} , suggesting that the nonlinearity between z_0
418 and H_{RMSE} in equation (6) may reflect a dependence of z_0 on S_{av} in addition to a dependence of z_0
419 on H_{RMSE} . This hypothesis is consistent with Figure 8C, which demonstrates that H_{RMSE} values
420 are highly correlated with S_{av} values, i.e. that, in the playa surfaces we studied, playas with larger
421 microtopographic amplitudes are systematically steeper. We would not expect such a correlation
422 between amplitude and steepness to apply to all landform types because, as microtopography
423 transitions into mesotopography and H_{RMSE} increase from 0.1 to 1 and higher, slope gradients do
424 not continually steepen without bound. If our goal is to understand the controls on z_0 values in
425 landscapes generally, the data in Figure 8 suggests that it is necessary to quantify the separate
426 controls of amplitude and slope on z_0 values. This was the purpose of the CFD modeling
427 described in the next section.

428 **3.3. Computational fluid dynamics**

429 To demonstrate the suitability of PHOENICS for modeling atmospheric boundary-layer
430 flows and to establish that the effective roughness length depends on the microtopographic
431 variability at multiple scales, we performed a numerical experiment using the central
432 microtopographic profile measured at the Soda Lake smooth site as input (plotted in Fig. 9A).

433 We measured a mean z_0 value of 4.6 mm from velocity profiles at this site. Figure 9B presents
434 the velocity profiles predicted by the PHOENICS model for 2D flow over the profile, following
435 the procedures detailed in the Methods section. PHOENICS predicts an effective roughness
436 length of 2.4 mm based on a least-squares fit of the velocity to the logarithms of distance above
437 the ground from a height equal to twice the height of the dominant roughness elements to the top
438 of the model domain. As such, the PHOENICS model predicts a z_0 value similar to the value we
439 measured in the field (relative to the four order-of-magnitude variation in z_0 values we measured
440 across the study sites).

441 To demonstrate that the z_0 value depends on microtopographic variability at multiple
442 scales, we filtered the Soda Lake smooth profile diffusively to remove some of the small-scale
443 (high-wavenumber) variability while maintaining the large-scale variability (i.e. the root-mean-
444 squared variability of the filtered and unfiltered profiles is identical). Figure 9 plots the original
445 profile, the filtered profile, and their amplitude and z_{0n} spectra. The z_0 values for the unfiltered
446 and filtered cases are 2.4 mm and 0.15 mm, respectively, based on fitting the velocity profiles
447 predicted by PHOENICS. That is, the filtered profile has a z_0 value more than an order of
448 magnitude smaller than the original profile despite the fact that the amplitude of the large-scale
449 microtopographic variations is the same as the original profile. Equation (4) predicts 2.8 mm and
450 0.25 mm, respectively, for the z_0 values. The z_0 value decreases in the filtered case because steep
451 slopes that trigger flow separation are significantly reduced at a wide range of scales by filtering,
452 lowering the z_0 value.

453 The results of this numerical experiment demonstrate that z_0 values depend on variability
454 microtopographic variability at multiple scales. There is also a general theoretical argument that
455 supports this conclusion. If one accepts that both the amplitude and slope of the microtopography

456 influence the effective roughness length (which we will demonstrate below for the case of a
457 sinusoid), it follows that there is no single Fourier mode that controls the effective roughness
458 length, unless the topography is a perfect sinusoid. This is because the slope is a high-pass filter
459 of the topography (i.e. the slope is proportional to $k \cdot a_n$ where a_n is the Fourier coefficient) and
460 hence is more sensitive to high-wavenumber components of the topography than the amplitude
461 is.

462 Figure 10 presents color maps that illustrate the output of the CFD model for an example
463 case ($a = 0.05$ m and $S = 0.79$ m/m). Figure 10A, which shows a color map of the turbulent
464 kinetic energy, illustrates the growth of the internal boundary layer with increasing distance from
465 the upwind boundary of the domain as the input velocity profile interacts with and adjusts to the
466 presence of the microtopography. Figures 10B&10C zoom in on the flow and illustrate the zones
467 of flow separation that occur in this example. These figures also illustrate the terrain-following
468 and logarithmically spaced nature of the computational grid in the vertical direction.

469 Figure 11 plots the z_0 values computed from an analysis of the CFD-predicted wind
470 profiles over sinusoidal topography for two different values of the sine-wave amplitude ($a = 0.05$
471 m and 0.1 m) and for a range of values of the maximum slope S from approximately 0.001 to 2.0.
472 For maximum slope values less than approximately 0.004, the z_0 value is equal to z_{0g} , as we
473 would expect (the topography is effectively flat). As the slope of the microtopography increases,
474 the wind field is increasingly perturbed by the roughness of the terrain. Eventually, flow
475 separation is triggered and flow recirculation zones are created in the wakes of each bedform,
476 further increasing z_0 values. For very steep slopes, i.e. $S \sim 0.4-1$, z_0 values still increase with
477 increasing slope but at a slower rate than for gentler slopes since the flow is already separated
478 and additional steepening has only a modest effect on the spatial extent of flow separation and z_0

479 values. The nonlinear dependence of z_0 on S is well fit by a sigmoidal relationship of the form
480 given by equation (4). Best-fit values are $c_1 = 0.1$, $c_2 = 0.4$, and $c_3 = 2.0$.

481 **3.4. Fourier analysis of topography and a multi-scale approach to quantifying z_0**

482 Using a minimization of the squared difference between the mean measured values of z_0
483 and the values predicted by equation (4) for all study sites, we found the optimal value of c_4 to be
484 1.5. Figure 12 plots z_{0n} values computed by equation (4) as a function of the natural
485 wavenumber, k . The sum of all the z_{0n} values is the predicted value of z_0 for each surface. There
486 is also value, however, in examining the dependence of z_{0n} on the wavenumber. The plot in
487 Figure 12 shows which spatial scales are most dominant in controlling the value of z_0 for a given
488 landscape (see arrows in Fig. 12). On Lordsburg Playa, the only spatial scales that have non-
489 negligible slope gradients are those at 0.01-0.3 m. At the rougher sites, the dominant roughness
490 elements are found at different scales, from 0.1-1 m (Soda Lake) to 1-10 m (Willcox Playa) to
491 0.3-3 m (Death Valley). This plot also shows that in some cases there is one dominant scale of
492 roughness elements (e.g. Soda Lake and Death Valley) while in others there are two or more
493 scales that are equally dominant (e.g. Willcox Playa).

494 Figure 13 plots the z_0 values predicted by equation (4) versus the mean measured values
495 for the ten study sites. Note that there appears to be only nine points plotted in Figure 13 because
496 two of the points (for Lordsburg smooth and Lordsburg intermediate) are nearly
497 indistinguishable. The correlation between the logarithms of the predicted and measured mean z_0
498 values is quite good ($R^2 = 0.991$). Equation (4) is capable of predicting z_0 values to 50%
499 accuracy, on average, across a four order-of-magnitude range.

500 An alternative approach is to use the values of H_{RMSE} and S_{av} to estimate z_0 using
501 equation (5). We found $c_5 = 16$ and $c_6 = 2.0$ to yield the highest R^2 value (0.978). Equation (5) is

502 thus a useful formula with an advantage of simplicity, but it is somewhat inferior to the multi-
503 scale analysis of equation (4) based on its lower R^2 value.

504

505 **4. Discussion and Conclusions**

506 The values of c_3 and c_2 respectively reflect the magnitude of the nonlinear increase in z_0
507 values as slope increases and the slope value where back-pressure effects begin to limit the rate
508 of increase in z_0 with increasing slope. The values of c_3 and c_6 (2.0) reflects a square relationship
509 between roughness length and the maximum slope of microtopographic variations at a given
510 scale, which is broadly consistent with the nonlinear relationship between z_0 values and
511 maximum slope in the model of Jacobs (1989) (note, however, that the Jacobs (1989) model
512 applies only to gentle slopes that do not trigger flow separation). The value of c_2 (0.4 or 24°) is
513 similar to the critical/maximum angle of attack of typical aerofoils (Bertin and Cummings,
514 2013). Critical angles of attack represent the maximum steepness possible before the drag effects
515 become greater than lift due to excessive pressure drag and the associated lee-side flow
516 separation. Similarly, the value of c_2 represents the maximum slope of the microtopography in
517 which an increase in slope leads to a nonlinear increase in z_0 values. Above this slope value, z_0
518 values increase more modestly with increasing slope because flow separation already occurs over
519 a significant portion over the surface.

520 The CFD model results demonstrate that equation (3) works well for a single sinusoid,
521 while equation (4) works well for real-world cases that can be represented as a superposition of
522 many (i.e., $N \gg 1$) sinusoids. The fact that the value of c_4 is larger than c_1 indicates that there is
523 no seamless transition between equation (3) and equation (4) as the topography changes from the
524 idealized case of a single sinusoid to the case of many superposed sinusoids. That is, neither

525 formula works well for the case of a small number of superposed sinusoids. The absence of such
526 a seamless transition could be a result of applying the superposition principle to a nonlinear
527 problem (boundary layer turbulence) for which it cannot apply precisely. In addition,
528 experimental studies demonstrate that flow separation (which influences z_0) is a function of both
529 the slope and the curvature of the bed (Simpson, 1989; Lamballais et al., 2010). Equations (3)
530 and (4) do not utilize curvature, hence neither equation can be the basis of a perfect method for
531 predicting z_0 . It is likely that the only way to precisely estimate z_0 is to compute the actual flow
532 field over the topography using a CFD model. Any other approach will likely involve some type
533 of approximation. We propose that equation (4), while imperfect, yields a good approximation
534 for z_0 values in real-world terrain (i.e. those with many Fourier coefficients contributing to z_0),
535 based on the R^2 value of 0.991 we obtained. Equation (5) provides an alternative for users who
536 prefer its simplicity. Equation (5) is not accurate for all possible S_{av} values, since z_0 cannot
537 increase without bound as S_{av} increases. As such, equation (5) should only be considered
538 applicable for microtopography with S_{av} values less than approximately 0.15.

539 We developed and tested a new empirical formula for the roughness length, z_0 , of the
540 fully rough form of the law of the wall that uses the amplitude and slope of microtopographic
541 variations across multiple scales within a discrete-Fourier-transform-based approach. A
542 sigmoidal relationship between z_0 and the amplitude and slope of sinusoidal topography
543 developed from CFD model results was used to quantify the effects of each scale of
544 microtopography on z_0 . The model was developed and tested using approximately sixty thousand
545 z_0 values from the southwestern U.S. obtained over 2.5 orders of magnitude in distance above the
546 bed. The proposed method is capable of predicting z_0 values to 50% accuracy, on average, across
547 a four order-of-magnitude range. This approach adds to our understanding of and ability to

548 predict the characteristics of turbulent boundary flows over landscapes with multi-scale
549 roughness.

550

551 **Data Availability**

552 DEMS of each of the study sites (relative elevation in m) and mean wind velocities (in m
553 s^{-1}) measured at seven heights above the ground at 12-s intervals are available as Supplementary
554 files.

555

556 **Acknowledgements**

557 This study was funded by award #W911NF-15-1-0002 of the Army Research Office. We
558 thank the staff of Death Valley National Park for permission to conduct a portion of the work
559 inside the park.

560

561 **References**

562 Arya, S. P. S.: A drag partition theory for determining the large-scale roughness parameter and
563 wind stress on the Arctic pack ice, *J. Geophys. Res.*, 80, 3447-3454, 1975.

564 Bagnold, R. A.: The movement of desert sand, *Proc. R. Soc. London, Set. A*, 157, 594–620,
565 1938.

566 Bauer B.O., Sherman, D.J., and Wolcott J.F.: Sources of uncertainty in shear stress and
567 roughness length estimates derived from velocity profiles, *Prof. Geogr.*, 44, 453–464,
568 1992.

569 Bergeron, N. E., and Abrahams, A. D.: Estimating shear velocity and roughness length from
570 velocity profiles, *Water Resour. Res.*, 28(8), 2155–2158, doi:10.1029/92WR00897, 1992.

571 Bertin, J. J., and Cummings, R. M.: Aerodynamics for Engineers, sixth edition, Prentice-Hall,
572 New York, 2013, 832 p.

573 Brown, O. W., and Hugenholz, C. H.: Quantifying the effects of terrestrial laser scanner settings
574 and survey configuration on land surface roughness measurement, *Geosphere*, 9(2), 367–
575 377, doi:10.1130/GES00809.1, 2013.

576 Counihan, J.: Wind tunnel determination of the roughness length as a function of the fetch and
577 the roughness density of three-dimensional roughness elements, *Atmos. Environ.*, 5(8),
578 637–642, doi:10.1016/0004-6981(71)90120-X, 1971

579 Dong, Z., Wang, X., Zhao, A., Liu, L., and Liu, X.: Aerodynamic roughness of fixed sandy
580 beds, *J. Geophys. Res.*, 106(6), 11,001-11,011, 2001.

581 Elliot, W. P.: The growth of the atmospheric internal boundary layer, *EOS Trans. AGU*, 38,
582 1048, 1958.

583 Gomez, B., and Church, M.: An assessment of bed load sediment transport formulae for gravel
584 bed rivers, *Water Resour. Res.*, 25, 1161–1186, 1989.

585 Hodge, R. A.: Using simulated Terrestrial Laser Scanning to analyse errors in high-resolution
586 scan data of irregular surfaces, *ISPRS J. Photogramm. Remote Sens.*, 65 (2), 227–240,
587 2010.

588 Jackson, P. S.: On the displacement height in the logarithmic velocity profile, *Journal of Fluid*
589 *Mechanics*, 111, 15–25, 1981.

590 Jacobs, S. L.: Effective roughness length for turbulent flow over a wavy surface, *J. Phys.*
591 *Oceanogr.*, 19, 998–1010, 1989.

592 Kean, J. W., and Smith, J. D.: Form drag in rivers due to small-scale natural topographic
593 features: 1. Regular sequences, *J. Geophys. Res.*, 111, F04009,
594 doi:10.1029/2006JF000467, 2006a.

595 Kean, J. W., and Smith, J. D.: Form drag in rivers due to small-scale natural topographic
596 features: 2. Irregular sequences, *J. Geophys. Res.*, 111, F04010,
597 doi:10.1029/2006JF000490, 2006b.

598 Lamballais, E., Silvestrini, J., and Laizet, S.: Direct numerical simulation of flow separation
599 behind a rounded leading edge: Study of curvature effects, *Inter. J. Heat Fluid Flow*, 31,
600 295-306, doi:10.1016/j.ijheatfluidflow.2009.12.007, 2010.

601 Lettau, H.: Note on Aerodynamic Roughness-Parameter Estimation on the Basis of Roughness-
602 Element Description, *J. Appl. Meteorol.*, 8, 828–832, doi:10.1175/1520-
603 0450(1969)008<0828:NOARPE>2.0.CO;2, 1969.

604 Ludwig, J. C.: PHOENICS-VR Reference Guide, CHAM Ltd., London, U.K., digital document
605 available online at <http://www.cham.co.uk/documentation/tr326.pdf>, 2011.

606 Nakato, T.: Tests of selected sediment-transport formulas, *J. Hydraulic Eng.*, 116, 362–379,
607 1990.

608 Namikas, S. L., Bauer, B. O., and Sherman, D. J.: Influence of averaging interval on shear
609 velocity estimates for aeolian transport modeling, *Geomorphology*, 53(3-4), 235–246,
610 2003.

611 Nield, J. M., et al.: Estimating aerodynamic roughness over complex surface terrain, *J. Geophys.*
612 *Res. Atmos.*, 118, 12,948–12,961, doi:10.1002/2013JD020632, 2014.

613 Patankar, S. V., and Spalding, D. B.: A calculation procedure for heat, mass and momentum
614 transfer in three-dimensional parabolic flows, *Inter. J. Heat Mass Transfer*, 15, 1782–
615 1806, doi:10.1016/0017-9310(72)90054-3, 1972.

616 Prigent, C., Tegen, I., Aires, F., Marticorena, B., and Zribi, M.: Estimation of the aerodynamic
617 roughness length in arid and semi-arid regions over the globe with the ERS scatterometer,
618 *J. Geophys. Res.*, 110, D09205, doi:10.1029/2004JD005370, 2005.

619 Raupach, M. R.: Drag and drag partition on rough surfaces, *Boundary Layer Meteorol.*, 60(4),
620 375–395, 1992.

621 Raupach, M. R.: Simplified expressions for vegetation roughness length and zero-plane
622 displacement as functions of canopy height and area index, *Boundary-Layer Meteorol.*,
623 71(1-2), 211–216, doi:10.1007/BF00709229, 1994.

624 Sherman, D. J., and Farrell, E. J.: Aerodynamic roughness length over movable beds:
625 Comparison of wind tunnel and field data, *J. Geophys. Res.*, 113, F02S08,
626 doi:10.1029/2007JF000784, 2008.

627 Simpson, R. L.: Turbulent boundary-layer separation, *Ann. Rev. Fluid Mech.*, 21, 205–234,
628 1989.

629 Smigelski, J. R.: Water level dynamics of the North American Great Lakes: Nonlinear scaling
630 and fractional Bode analysis of a self-affine time series, unpublished Ph.D. dissertation,
631 Wright State University, 890 p., 2013.

632 Smith, J. D., and McLean, S. R.: Spatially averaged flow over a wavy surface, *J. Geophys. Res.*,
633 82(12), 1735–1746, 1977.

634 Spalding, D. B.: *Mathematical Modelling of Fluid-Mechanics, Heat-Transfer and Chemical-*
635 *Reaction Processes*, CFDU Report HTS/80/1, Imperial College, London, 1980.

636 Taylor, P. A., Sykes, R. I., and Mason. P. J.: On the parameterization of drag over small-scale
637 topography in neutrally-stratified boundary-layer flow, *Bound. Layer Meteor.*, 48(4),
638 409–422, 1989.

639 Yakhot, V., and Orszag, S. A.: Renormalization group analysis of turbulence, *J. Sci. Comput.*, 1,
640 3–51, doi:10.1007/BF01061452, 1986.

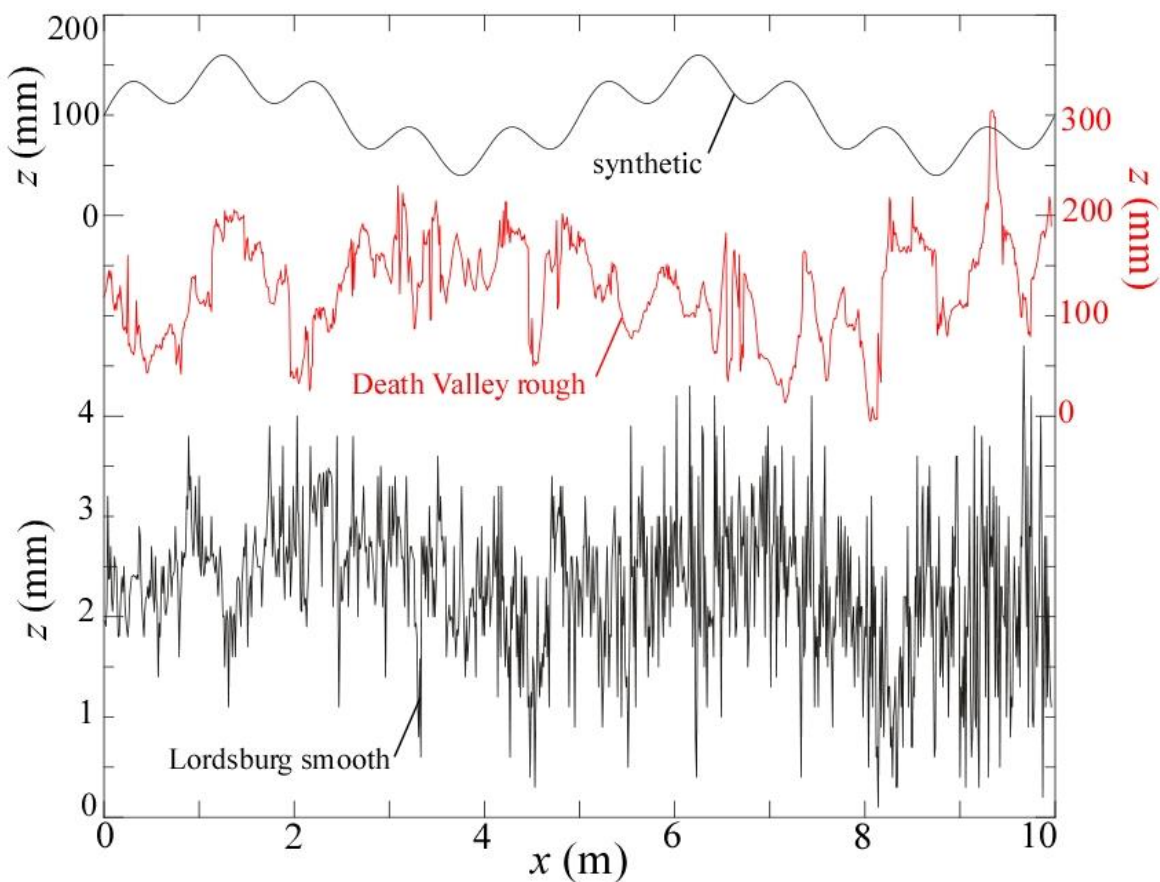
641 Yakhot, V., Orszag, S. A., Thangam, S., Gatski, T. B., and Speziale, C. G.: Development of
642 turbulence models for shear flows by a double expansion technique: *Phys. Fluids A*, 4(7),
643 doi: 10.1063/1.858424, 1992.

644

645 Table 1. Study site locations, attributes, and predictions of Eqs. (4) and (5).

Name	Latitude (° N)	Longitude (° W)	# profiles	H_{RMSE} (mm)	S_{av}	mean z_0 (mm)	pred. z_0 Eq. (4) (mm)	pred. z_0 Eq. (5) (mm)
Death V. rough	36.34449	116.86338	8036	34	0.144	23	34	11
Death V. interm.	36.34466	116.86321	10922	36	0.142	16	26	12
Death V. smooth	36.34485	116.86307	9457	26	0.122	6.3	10	6.2
Soda Lake rough	35.15845	116.10413	10838	14	0.159	7.6	4.1	5.7
Soda Lake smooth	35.15852	116.10352	7134	11	0.154	4.6	2.8	4.2
Willcox rough	32.16882	109.88889	6404	6.6	0.056	0.26	0.22	0.33
Willcox smooth	32.14869	109.90317	2403	4.8	0.076	0.16	0.14	0.44
Lordsburg rough	32.28137	108.88378	1883	1.3	0.032	0.047	0.020	0.021
Lordsburg interm.	32.28105	108.88400	2569	0.72	0.017	0.002	0.0026	0.0033
Lordsburg smooth	32.28097	108.88459	203	0.55	0.017	0.002	0.0025	0.0025

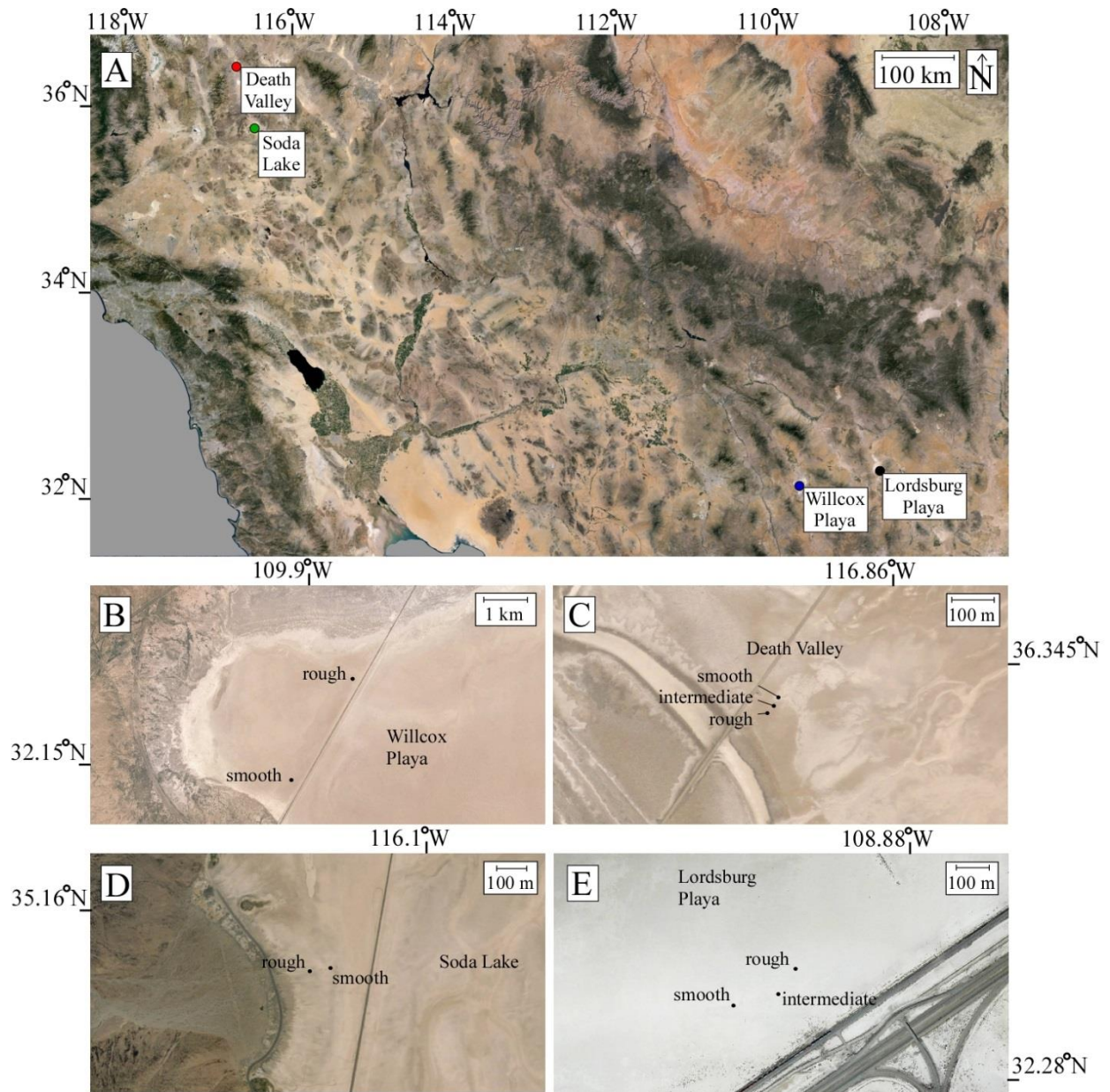
646



647

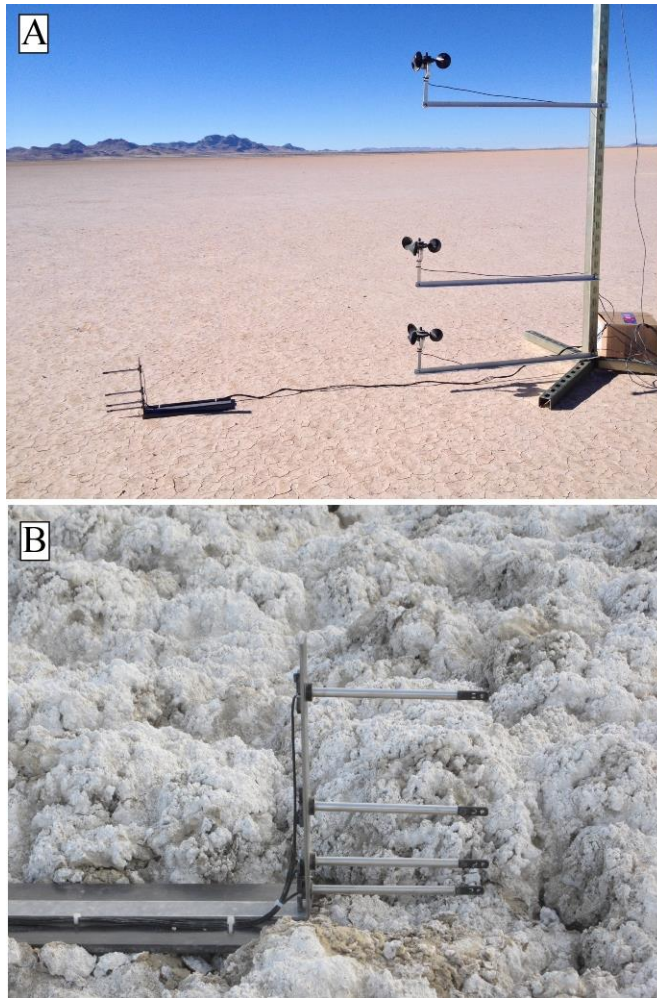
648 Figure 1. Plots of synthetic (top) and real (middle and bottom) topographic transects illustrating

649 the multi-scale nature of topography using natural playa surfaces as examples.



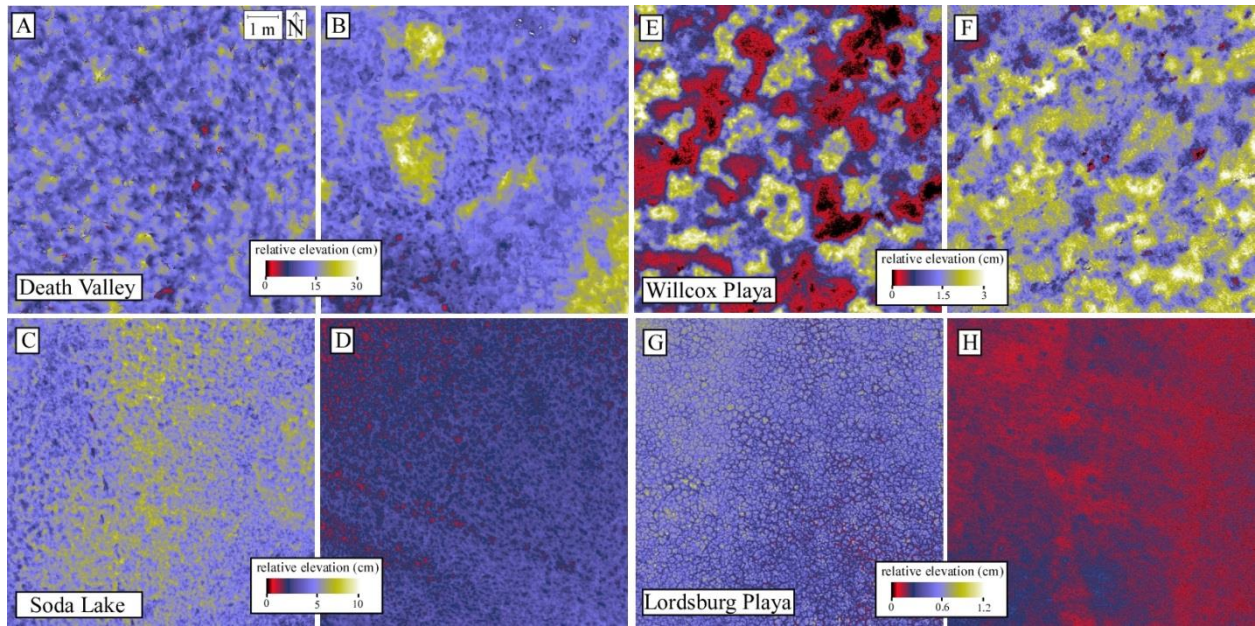
650

651 Figure 2. Aerial images of the study sites.



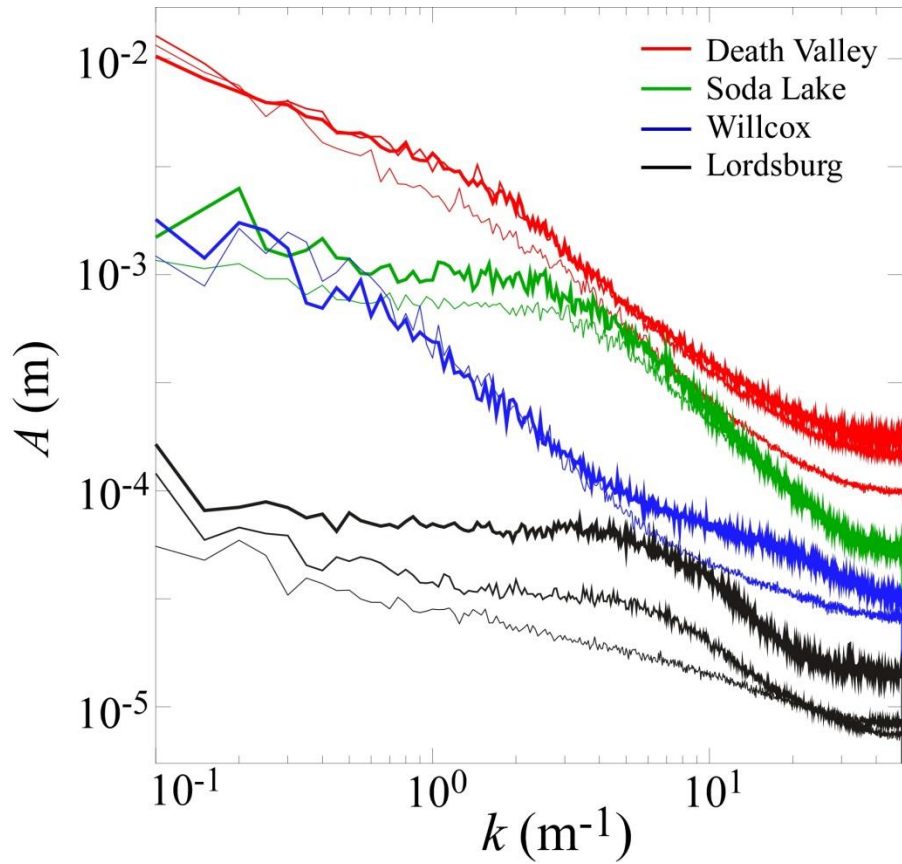
652

653 Figure 3. Photographs of the equipment used for measuring wind profiles. (A) Mast holding 4
654 hot-wire anemometers (left) and four cup anemometers (right, note that only the lowest 3 are
655 visible) at the Animas intermediate study site. (B) Close-up photograph of the hot-wire sensors at
656 the Soda Lake smooth site. For scale, note that the top hot-wire sensor is located 0.16 m above
657 the surface in both photographs.



658

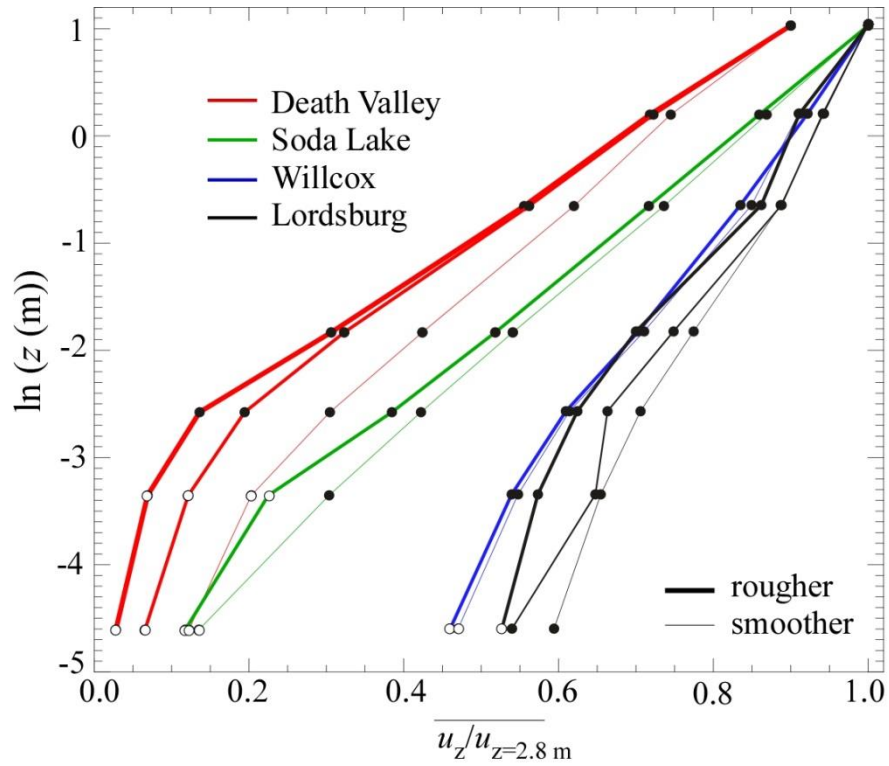
659 Figure 4. Color maps of TLS-derived DEMs of eight of the ten study sites. (A) Death Valley
 660 rough, (B) Death Valley smooth, (C) Soda Lake rough, (D) Soda Lake smooth, (E) Willcox
 661 rough, (F) Willcox smooth, (G) Lordsburg rough, (H) Lordsburg smooth. Note the differing
 662 color scales between (A)&(B) and (C)&(D).



663

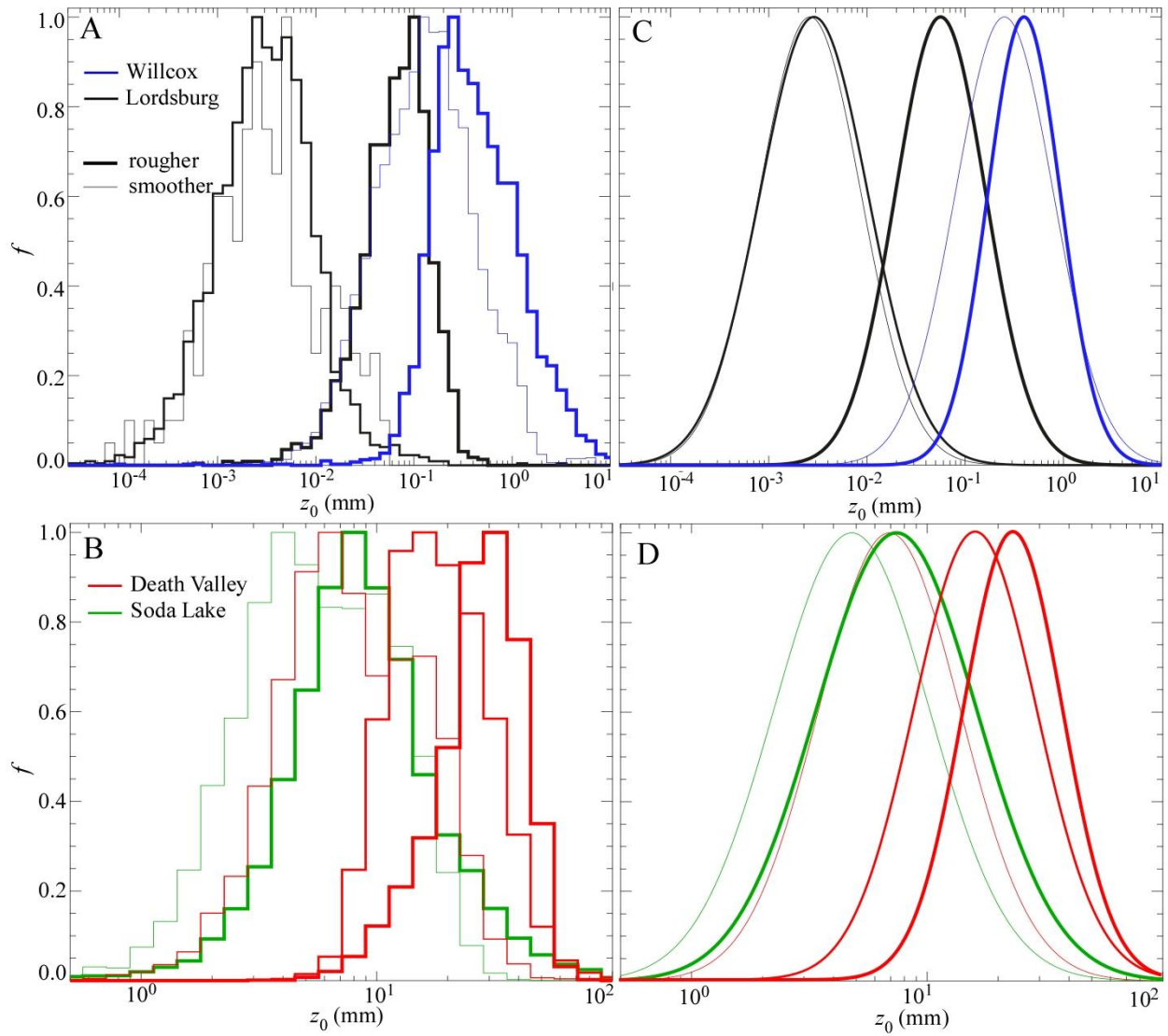
664 Figure 5. Plots of the average amplitude spectrum, A , of 1D transects of the microtopography of
 665 each site as a function of the natural wavenumber, k . The colors red, green, blue, and black are
 666 used to represent the Death Valley, Soda Lake, Willcox, and Lordsburg sites, respectively.

667 Thicker curves represent rougher sites within each playa.



668

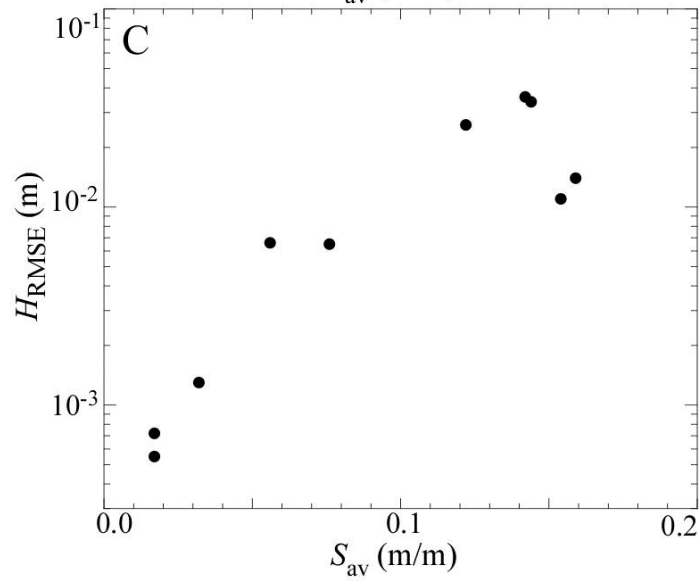
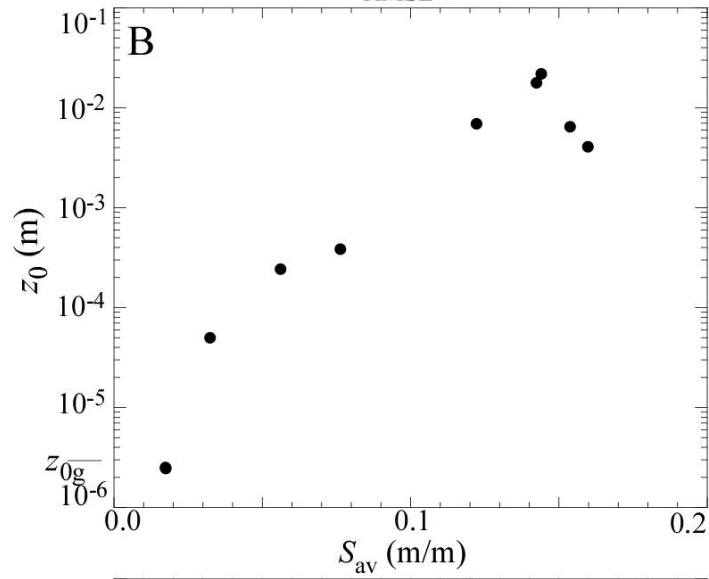
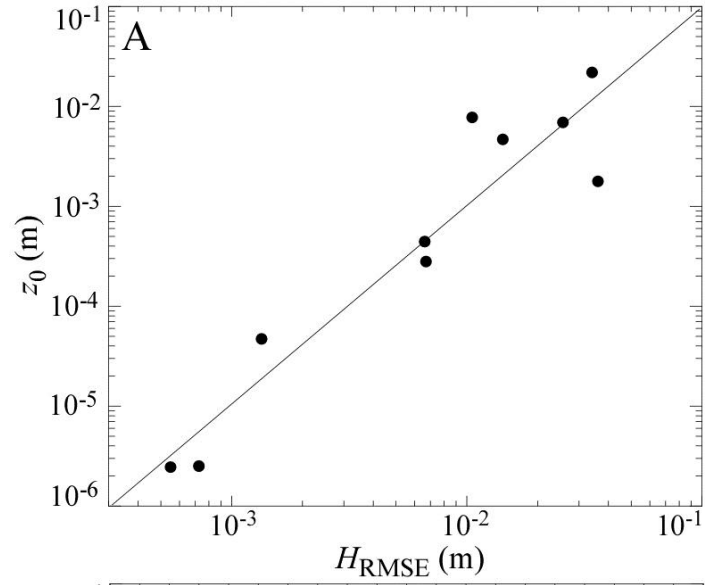
669 Figure 6. Plots of mean wind velocity (normalized by the velocity measured at the highest
 670 sensor, located 2.8 m above the ground) (x axis) as a function of the natural logarithm of height
 671 above the ground (y axis). The colors red, green, blue, and black are used to represent the Death
 672 Valley, Soda Lake, Willcox, and Lordsburg sites, respectively. Within each playa, thicker lines
 673 are used to represent the rougher sites. Open circles indicate stations located within the
 674 roughness sublayer. These sensors were not used to calculate z_0 .



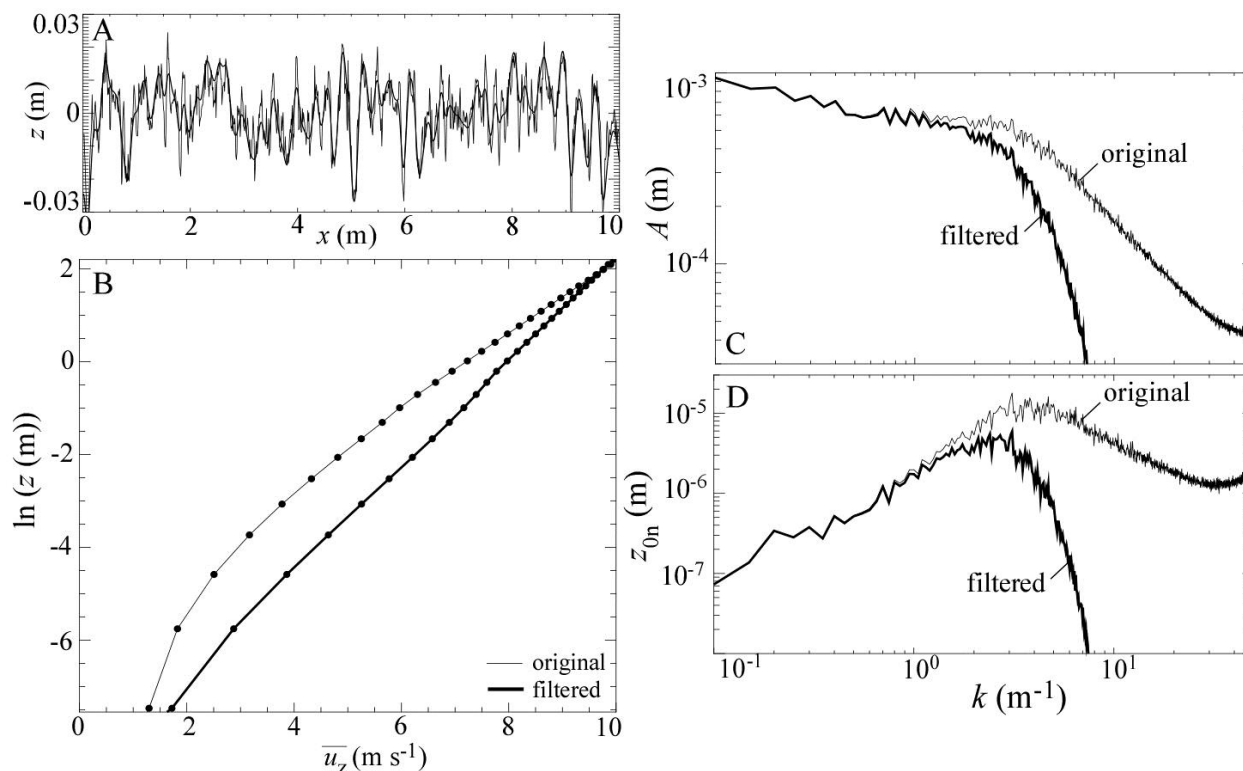
675

676 Figure 7. (A)-(B) Normalized histograms of z_0 values measured at each site and (C)-(D)

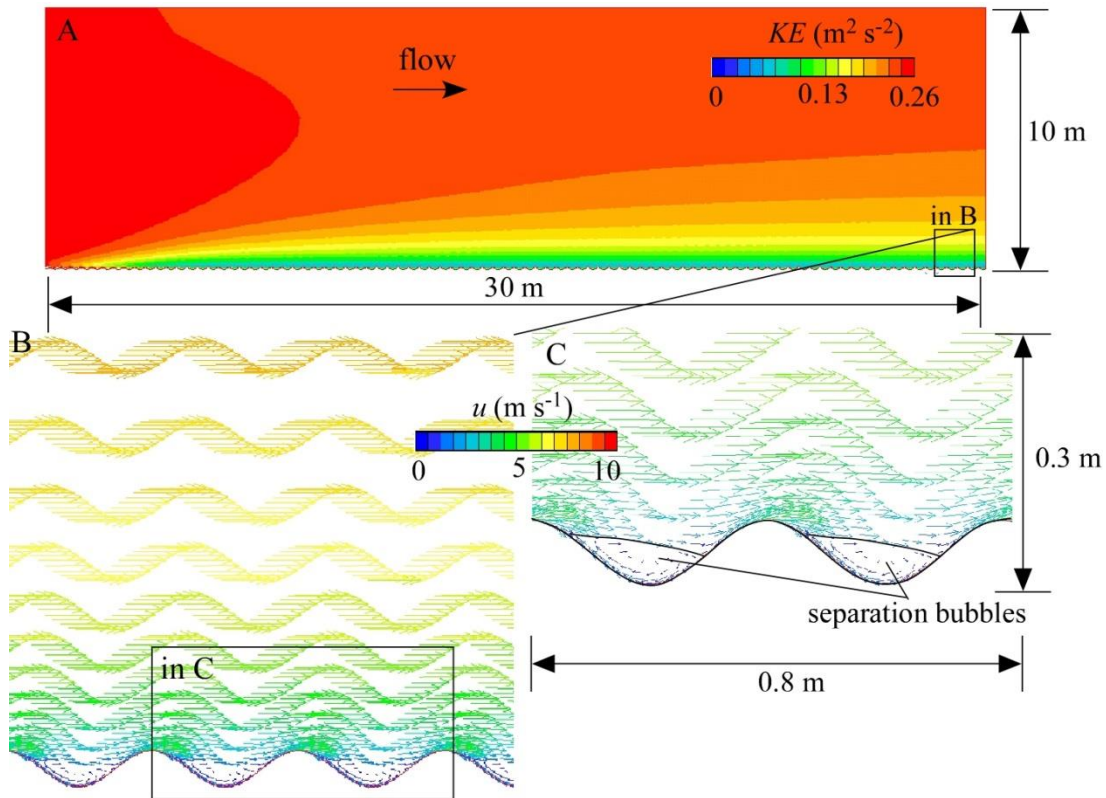
677 probability distributions for each site, assuming z_0 values are log-normally distributed.



679 Figure 8. Plots of mean z_0 at each site versus (A) H_{RMSE} and (B) S_{av} . (C) Plot of H_{RMSE} vs. S_{av} .

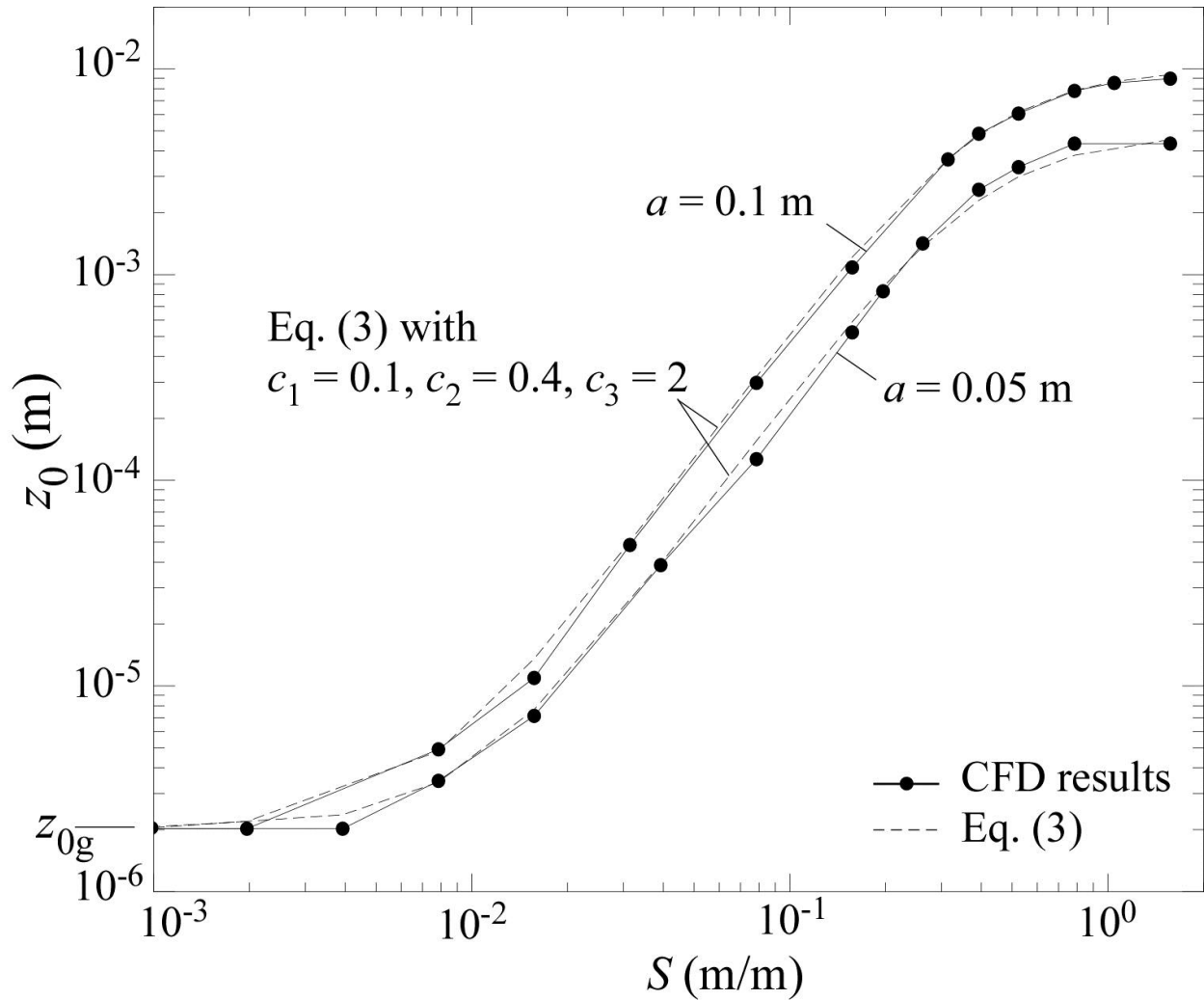


680
 681 Figure 9. Demonstration of the dependence of z_0 values on the multi-scale nature of
 682 microtopography. (A) Plot of a profile through the Soda Lake smooth site (thin curve). Also
 683 shown is the same plot with diffusive smoothing (thicker curve). Smoothing maintains the
 684 amplitude of microtopographic variations at large spatial scales (i.e. the amplitude spectrum is
 685 unchanged at large scales) but removes some of the small-scale (high-wavenumber) variability.
 686 (B) Plots of the mean velocity profiles predicted by PHOENICS over the original and filtered
 687 profile. (C) Amplitude spectra of the two plots in (A). (D) Contributions of each Fourier mode to
 688 the z_0 values for the two plots in (A).



689

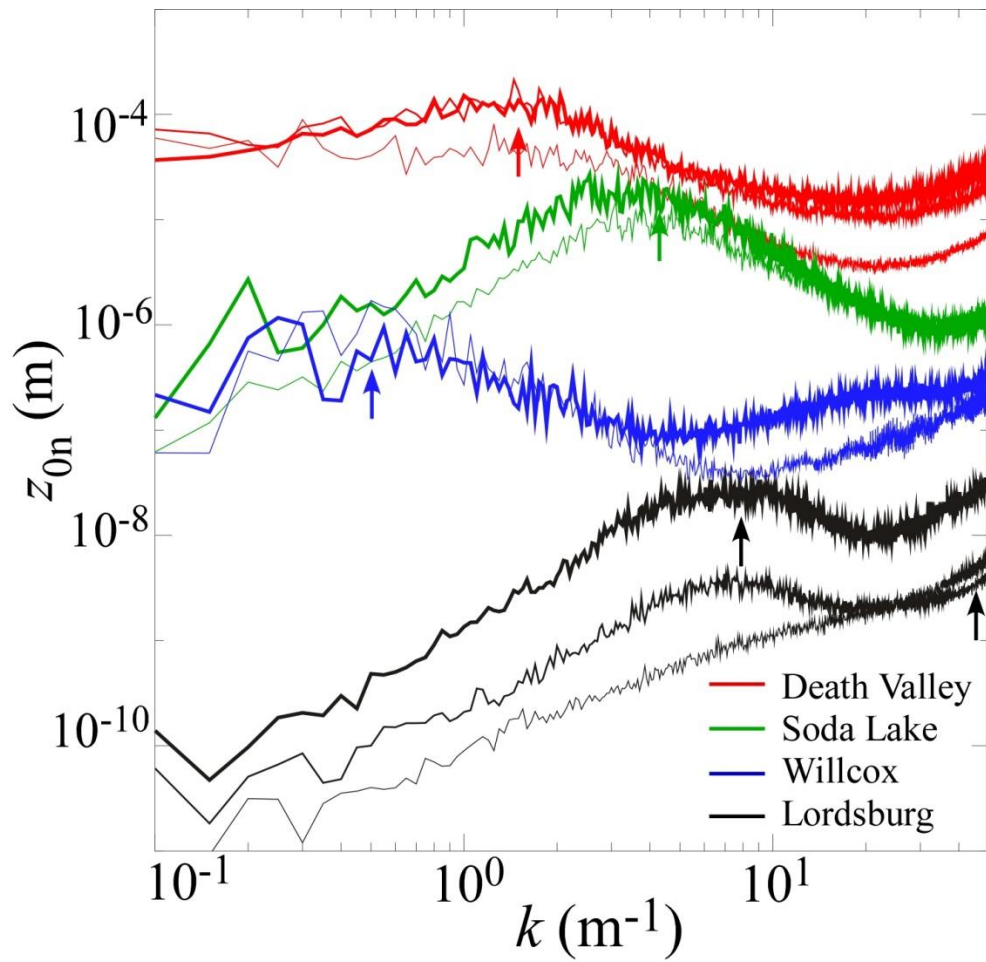
690 Figure 10. Illustrations of the output of the PHEONICS CFD model for the example case (with
 691 amplitude $a = 0.05$ m and maximum slope $S = 0.79$ m/m) of flow over a sinusoidal bed. (A)
 692 Color map of turbulent kinetic energy, KE . This map illustrates the growth of the internal
 693 boundary layer triggered by the effective roughness change as the input velocity profile
 694 (characterized by a grain-scale roughness z_{0g}) interacts with and adjusts to the microtopography.
 695 The color vector maps in (B) and (C) illustrate the zones of flow recirculation that occur in the
 696 lee side of each bedform.



697

698 Figure 11. Plot of the z_0 value predicted by the PHOENICS CFD model for flow over sinusoidal
 699 terrain with two values of the amplitude, a , and a wide range of values of the maximum slope
 700 values, S . Also shown are predictions of Eq. (3) for the best-fit parameter values.

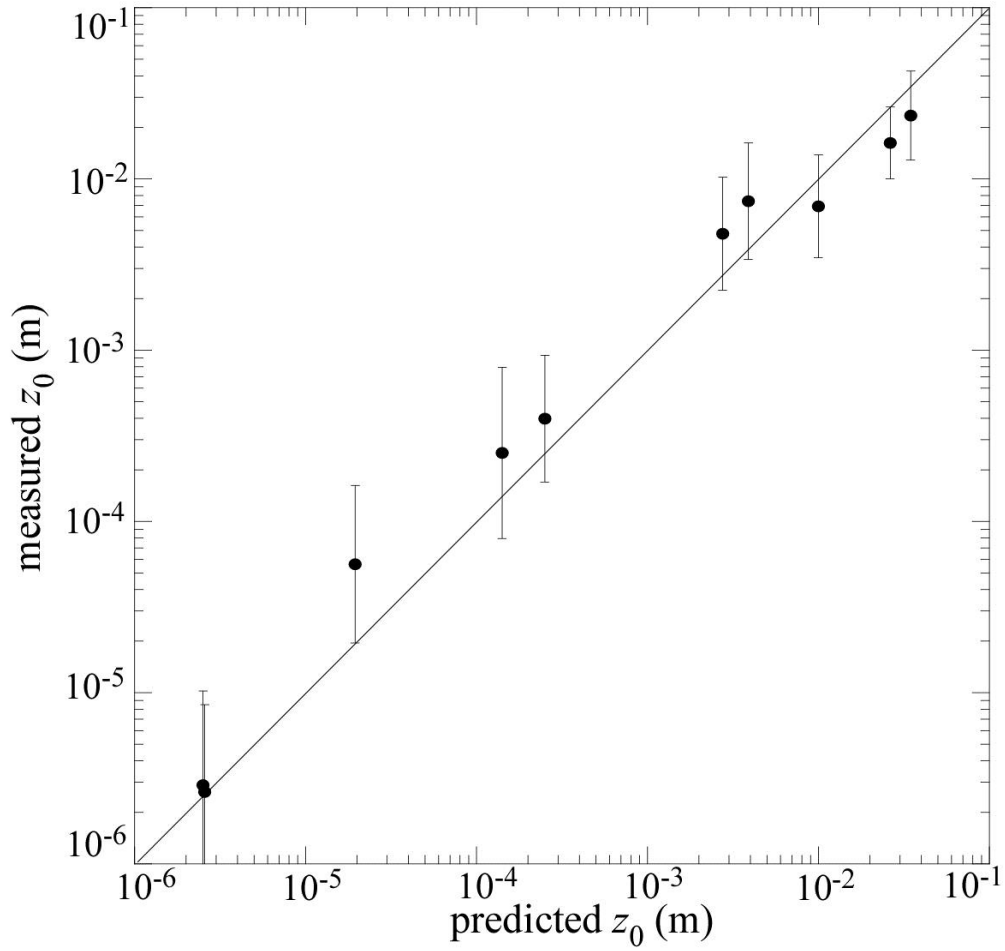
701



702

703 Figure 12. Plots of the contribution of each Fourier mode to the effective roughness length, z_{0n} ,

704 as a function of k . Arrows point to the range of wavenumbers that contribute most to z_0 .



705

706 Figure 13. Plot of mean measured z_0 values versus predicted values (using Eq. (4)) for the ten

707 study sites. Error bars denote 1σ variations in the measured z_0 values.